




High-responsivity operation of quantum cascade detectors at 9 μm

G. MARSCHICK,^{1,5} M. DAVID,¹  E. ARIGLIANI,¹ N. OPAČAK,¹ 
B. SCHWARZ,¹  M. GIPARAKIS,¹ A. DELGA,² M. LAGREE,²
T. POLETTI,² V. TRINITE,² A. EVIRGEN,² B. GERARD,² G. RAMER,³
R. MAULINI,⁴  J. BUTET,⁴ S. BLASER,⁴ A. M. ANDREWS,¹ 
G. STRASSER,¹  AND B. HINKOV^{1,6} 

¹Institute of Solid State Electronics and Center for Micro- and Nanostructures, Technische Universität Wien, Vienna, Austria

²III-VLab, a joint Thales, Nokia and CEA-LETI laboratory, Palaiseau, France

³Institute of Chemical Technologies and Analytics, Technische Universität Wien, Vienna, Austria

⁴Alpes Lasers SA, St-Blaise, Switzerland

⁵georg.marschick@tuwien.ac.at

⁶borislav.hinkov@tuwien.ac.at

Abstract: Quantum cascade detectors (QCDs) are devices operating at zero external bias with a low dark-current. They show linear detection and high saturation intensities, making them suitable candidates for heterodyne detection in long-wave infrared (LWIR) free space optical communication systems. We present an approach to mitigate the performance limitation at long wavelengths, by a comparison of similar single and multi-period QCDs for optimizing their responsivity and noise behaviour. Our InGaAs/InAlAs/InP ridge QCDs are designed for operation at $\lambda = 9.124 \mu\text{m}$. Optical waveguide simulations support the accurate optical characterization. A detailed device analysis reveals room-temperature responsivities of 111 mA/W for the 15-period and 411 mA/W for the single-period device.

Published by Optica Publishing Group under the terms of the [Creative Commons Attribution 4.0 License](https://creativecommons.org/licenses/by/4.0/). Further distribution of this work must maintain attribution to the author(s) and the published article's title, journal citation, and DOI.

1. Introduction

The mid-infrared spectral region is the portion of the electromagnetic spectrum, that is highly suitable for spectroscopy of gases and liquids by addressing their fundamental bending and stretching vibrations [1,2]. It also hosts multiple atmospheric transmission windows, extending to the long-wavelength infrared (LWIR). Especially, the low susceptibility towards atmospheric turbulences and small attenuation in the LWIR [3], together with the fast modulation capabilities of intersubband devices [4,5], make this spectral range highly promising for unlocking novel telecom applications [5,6]. One crucial component in telecommunication receiver systems are suitable high-performance detectors. While HgCdTe-based interband photodetectors (MCTs) are very sensitive, moderate bandwidth (low-GHz range) detectors, they have low saturation thresholds, limiting their application in heterodyne detection. MCTs are in particular not suitable for monolithic integration due to their incompatible material system. In contrast, photoconductive quantum well infrared photodetectors (QWIPs) [7,8], show high responsivities and improved high frequency behaviour ($\gg 10$ GHz) [9], due to short intrinsic carrier lifetimes. One major drawback of QWIPs is their pervasive dark current, originating from biased detector operation [10]. Quantum cascade detectors (QCDs), demonstrated in 2002, support high-speed and room temperature operation [11,12]. Based on QC laser (QCL) structures relying on intersubband transitions, they allow unbiased, i.e. low dark-current, detection, opening pathways for low-noise

applications [13]. Even more important for compact heterodyne detection is their linearity and high saturation intensity [2]. The realization of monolithic devices, integrating active and passive components like lasers, detectors and waveguides on one chip, makes them suitable for sensing and telecommunication applications [14–16]. Extending the telecom-bandwidth to mid-infrared frequencies mitigates bandwidth and availability limitations in current fifth generation (e.g. Long-Term Evolution (LTE)) communication systems, arising from demanding high-speed breakthrough technologies like unmanned mobility, industry 4.0, e-health [17,18] and satellite communication [19]. Moreover, mid-infrared free space optical links have small device footprints, low power consumption and high modulation speeds [20,21] with high connection stability and reliability even under harsh weather conditions including fog and rain. Literature shows that systems operating in the 8-12 μm atmospheric window are suitable candidates for such systems [22], but limited due to device performance at longer wavelengths and need further improvements. QCL devices covering this wavelength range were already successfully used as atmospherically robust transmitter units [23–26]. The first 9 μm QCDs operating at room temperature took advantage of the GaAs/AlGaAs material system [5]. We present room-temperature InGaAs/InAlAs ridge QCDs at this wavelength and show an experimental comparison between similar single and multi-period QCDs in our study. The reduction of the number of periods, in order to increase the device responsivity and its impact on the noise behaviour, is an important parameter to optimize QCDs for implementation into monolithic heterodyne detectors.

2. Device design and fabrication

In this work, we demonstrate two different QCDs designed for the target wavelength of 9.124 μm : 1) a 15-period device with high-specific-detectivity, and 2) a high-responsivity single-period device. The facet-illuminated ridge devices are optimized for low-noise, high-responsivity operation. This geometry is required for the development of a monolithic photonic integrated circuit (PIC) device [27,28]. For monolithical integration of active and passive components, as for example needed for a heterodyne detection system, ridge geometry can be directly implemented. Laser, waveguide, and detector can be fabricated aligned to each other on a single chip, preventing difficult alignment procedures between components. A trade off between the optical active area and the effective electric area has to be found. Small electrical areas lead to high device resistivities and thus improve the signal to noise ratio (SNR) while large optical areas increase the device response. Mesa structures, illuminated from the top-side, show the same size of electrical and optical area while the optical area can be increased through different structures, like photonic crystal cavities or plasmonic lenses [29,30]. Ridge devices, on the other hand, can be fabricated narrow and short, reducing the electrical active area. By incoupling light from the side facet, optimal absorption lengths are ensured even though the optical active area is small compared to mesa-geometries [31,32]. Further, light polarized in growth direction can be directly detected without additional gratings [33], compared to, for example, surface detecting devices [34]. One of the most commonly used material systems in mid-IR and terahertz photonics is InGaAs/InAlAs, lattice matched to InP substrate. We used the same material system in this work grown by molecular beam epitaxy (MBE). The alternating stacking of InGaAs and InAlAs creates a series of quantum wells, forming energy bands through the coupling of the individual energy states. One period is typically referred to as the part of the active region that contains the optical active quantum well together with the extractor/injector sections transporting the electrons from one active region period to the next. The extraction mechanism is a reason why QCDs are highly suitable candidates for data transmission: the lifetime of the typically involved LO phonons is < 1 ps, making QCDs fast devices with very high saturation thresholds [35]. QCDs are typically realized with 5 to 50 periods in their active region, with exceptions like single period devices [36] as in this work. The simulated band structures were obtained via a

self-consistent calculation scheme of the eight-band $k \cdot p$ model and the Poisson equation [37,38]. As the former yields the subbands spatial distribution based on the band structure, the latter finds the corresponding Fermi levels with consideration of the dopant densities. The Hartree potentials are calculated as the electrostatic potential of the electron charge densities. Figure 1 shows the simulated band structure of the single period device at room temperature and at zero-bias operation. The optical transition occurring in the active well is indicated by the red arrow, while the current flow through the device is indicated by the black arrows. The active zone is embedded in a waveguide and composed as follows (**InAlAs** layers in bold, Si-doped layers underlined, in nanometers): **2.5**, 7.2, **2.5**, 6.6, **2.5**, 6.6, **3.5** ($2 \times 10^{17} \text{ cm}^{-3}$), 9.4 ($8 \times 10^{17} \text{ cm}^{-3}$), **4.5**, 3.3, **4.1**, 3.5, **4.1**, 4.1, **3.4**, 4.4, **3.4**, 5, **3**, 6.5, **3** ($3 \times 10^{17} \text{ cm}^{-3}$). The layer sequence of the active region stack, including the injector/extractor structure of the 15 period device in nanometers is **4.5**, 3.2, **4.3**, 3.3, **3.9**, 3.5 ($1 \times 10^{17} \text{ cm}^{-3}$), **3.9**, 3.8, **4.1**, 4.4, **3.7**, **3.7**, 4.7, 5.1, **3.7**, 5.3, **2.8** ($1 \times 10^{17} \text{ cm}^{-3}$), 9.4 ($2 \times 10^{17} \text{ cm}^{-3}$), with **InAlAs** barrier layers in bold and Si-doped layers underlined. In Fig. 2, a cutout showing one period (between the dashed lines) of the simulated bandstructure of the multiperiod design, is depicted. This stack is repeated 15 times and embedded in a top, and bottom charge balancing region, easing the formation of ohmic contacts. In both designs, the series resistances of the bulk InGaAs/InP interfaces were reduced by the implementation of a contact chirped superlattice structure. Figure 1 and 2 allow a quantitative explanation of how the number of periods used in a design, will finally influence the detector performance and its figures of merit. The responsivity R of a QCD, the figure of merit describing the produced photocurrent per incoupled optical power, is proportional to $1/N$, with N being the number of periods [10]. On the other hand, a higher number of periods will increase the device resistance, improving its noise behaviour. This trade-off is the typical challenge in QCD design. The devices used in this work were fabricated as 200- μm -long and 14- μm -wide ridges, with a height of approximately 7 μm . After patterning the ridges with UV lithography and reactive ion etching (RIE), the surface was passivated with SiN using plasma enhanced chemical vapor deposition (PECVD). The devices were electrically contacted through a sputtered layer of titanium as an adhesion promoter, and gold. After cleaving to produce clean facets, the device was soldered to a copper base plate and bonded to a printed circuit board. Figure 3 shows a SEM picture of the cleaved facet of a 15-period detector ridge with indicated layers. The active region can be seen as the rectangle in a slightly brighter grey tone compared to the surrounding cladding layers. The SiN passivation

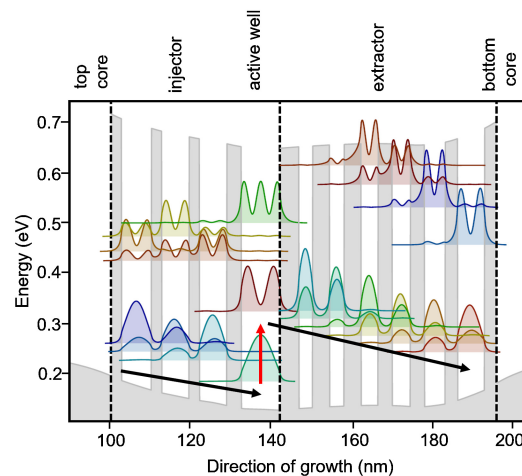


Fig. 1. Band structure of the single period design. The current path is visualized by the black arrows while the optical transition is pointed out by the red arrow.

layer can be identified as a dark, nearly black line between the substrate and the gold contact layer. The quality of the cleaved facet is a crucial parameter, determining the effectivity of incoupling the light.

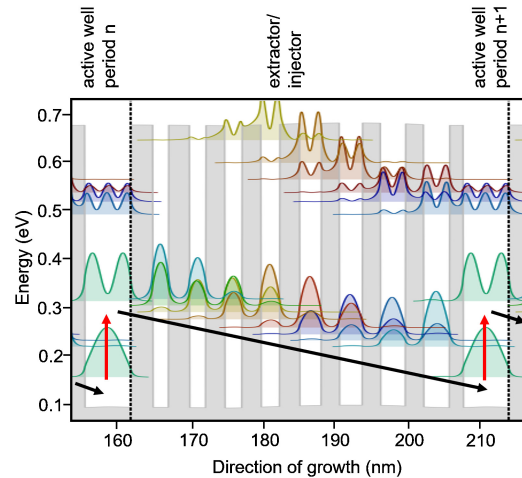


Fig. 2. Band structure of the 15-period design. The vertical dotted lines indicate the layers of one single period, which is repeated 15 times. The black arrows show the current path while the optical transitions are highlighted by the red arrows.

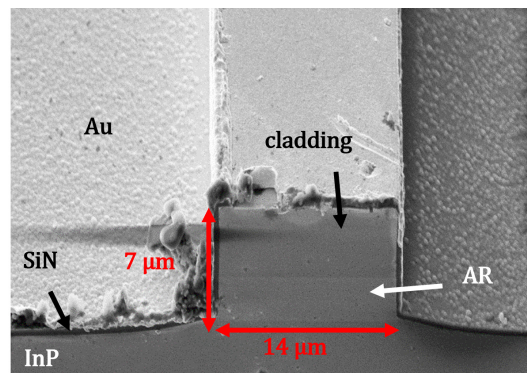


Fig. 3. Scanning electron microscope picture of the facet of a 15-period device. The individual layers are indicated.

3. Characterization

Both samples were characterized optically and electrically. I-V curves were measured with a Keithley 2601B source-meter for different device temperatures under dark conditions in order to extract the differential resistance at zero bias R_0 . For the plotted I-V curves we refer the reader to Figures S1 in the supplementary material. The extracted zero bias resistance $R_0 = dV/dI$ was plotted on a logarithmic scale as function of the inverse measurement temperature. The slope of the resulting curve in the arrhenius plot, shown in Fig. 4 describes the activation energy of the quantum well structure, and thus its transition energy. We extracted activation energies of $E_{A15-per} = 111.3$ meV for the 15-period device and $E_{Asingle} = 126.1$ meV for the single period

device, respectively. The low room-temperature resistances of $18\ \Omega$ and $264\ \Omega$ of the single period device and the 15-period device, respectively, can be explained by the low transition energy at a wavelength of $9.124\ \mu\text{m}$. Using a single period design lowers the resistance by simply reducing the number of subsequent barriers. The spectral characterization of the devices was conducted with an external-cavity QCL in pulsed operation, able to cover a wavelength range from $8 - 12\ \mu\text{m}$. Absolute responsivity measurements were done with an Alpes Lasers QCL in continuous wave operation at a wavelength of $9.28\ \mu\text{m}$. After the laser beam shape measurement and power calibration with the help of an automatized X-Y stage and an optical powermeter, the spectral responsivity curves were recorded at room temperature using a transimpedance- and a lock-in amplifier and scaled to the absolute values measured at $9.28\ \mu\text{m}$. To examine the free-space detector coupling and calculate the incoupled optical power with high precision, FEM simulations were performed. Figure 5 illustrates the spatial distribution of the optical mode intensity for the two QCD designs extracted with the simulation software COMSOL Multiphysics. The detector ridge structures were modeled according to the waveguide design. The effective mode area (A_{eff}) was calculated from the simulations as shown in Eq. (1),

$$A_{eff} = \frac{\left[\int_{-\infty}^{\infty} |E|^2 dA \right]^2}{\int_{-\infty}^{\infty} |E|^4 dA}, \quad (1)$$

where E is the electric field amplitude. The mode areas calculated at a wavelength of $\lambda = 9.124\ \mu\text{m}$ are $36.06\ \mu\text{m}^2$ and $41.15\ \mu\text{m}^2$ for the single period and 15-period device, respectively. Despite having only one active period, the single period device shows a similar optical active area as the mode is confined in the thicker waveguide claddings for this design. The substrate is not a relevant factor for light coupling, due to its high doping density ($10^{17}\ \text{cm}^{-3}$) and the strong impact of free-carrier absorption [39]. The simulations of the optical areas offer an accurate normalization factor for the incoupled power with relatively high precision. The optical coupling coefficient is assumed to be unity. This further means that our results represent rather conservative values as the incoupled power might be lower. Figure 6 shows the spectral responsivity curves of both detector designs at room temperature. We can see that the responsivity peak at $\lambda_{Rp} = 9.42\ \mu\text{m}$ of the single period device is slightly off the targeted wavelength of $\lambda_T = 9.124\ \mu\text{m}$ while the 15-period devices responsivity peaks exactly at λ_T . With a laser power of $P_{Laser} = 13.5\ \text{mW}$ measured after the ZnSe lens, used to focus the beam, the calculated incoupled power to the 15-period device was $P_{in-15} = 8.61\ \mu\text{W}$ and $P_{in-1} = 5.85\ \mu\text{W}$ to the single-period device. Peak responsivities of $R_p = 0.411\ \text{A/W}$ and $R_p = 0.111\ \text{A/W}$ were extracted from the single period device and the 15-period device, respectively. At λ_T , the single period device shows a room temperature responsivity of $R_{\lambda_T} = 0.279\ \text{A/W}$. The reached peak responsivities correspond to external quantum efficiencies of 5.4% and 1.5% for the single-period and the 15-period device respectively. The extraction efficiency was assumed to be unity in this calculation. The measured properties, responsivity and zero bias differential resistance, were used to obtain the specific Johnson detectivity, a figure of merit describing the Johnson noise behavior of the detector device. Specific detectivities of $D_{J-1}^* = 6.33 \cdot 10^7$ Jones for the single-period device's very low and $D_{J-15}^* = 6.54 \cdot 10^7$ Jones for the 15-period device were calculated. As in the case of monolithic waveguide integration the signal does not scale with the detector area (direct end-fire coupling), the noise equivalent power (NEP), which is not normalized on the detector area, is a more meaningful quantity. The corresponding noise equivalent powers at room temperature are $NEP_1 = 83.6\ \text{pW}/\sqrt{\text{Hz}}$ and $NEP_{15} = 80.9\ \text{pW}/\sqrt{\text{Hz}}$ for the single period and the 15-period device, respectively.

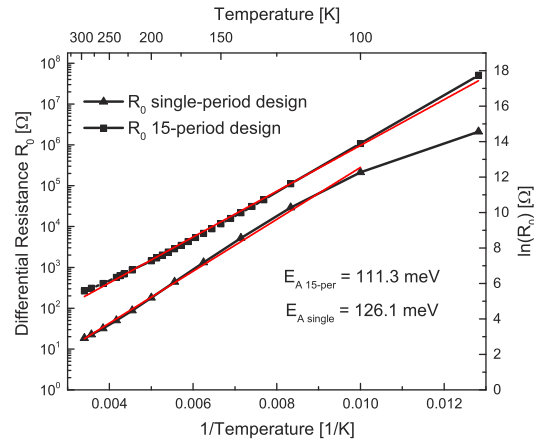


Fig. 4. Arrhenius plot: natural logarithm of the differential zero bias resistance plotted as a function of the reciprocal temperature. The slope of the curves is proportional to the activation energy E_A .

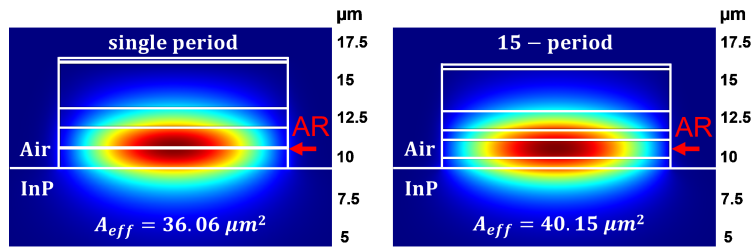


Fig. 5. Simulation of the spatial distribution of the optical mode intensity inside the waveguide. The active regions are highlighted by the red arrows.

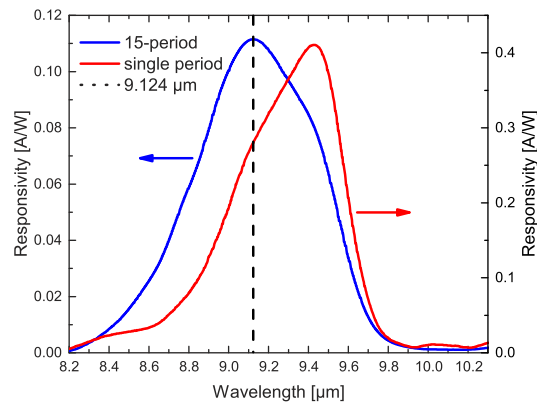


Fig. 6. Spectral responsivity curves acquired at room temperature. The 15-period device is shown in blue, the single period device is shown in red. The black dashed line marks the target wavelength of 9.124 μm .

4. Conclusion

Concluding our work, we designed, fabricated and characterized two different types of quantum cascade detectors, targeting a wavelength of $9.124\ \mu\text{m}$. As expected, the single period device shows a higher peak responsivity of $R_p = 0.411\ \text{A/W}$ compared to the 15-period device with $R_p = 0.111\ \text{A/W}$. Due to the single-period devices very low resistance, it shows a slightly higher noise equivalent power of $NEP_1 = 83.6\ \text{pW}/\sqrt{\text{Hz}}$ compared to the 15-period device with $NEP_{15} = 80.9\ \text{pW}/\sqrt{\text{Hz}}$, at room temperature. Device characterization, particularly the normalization of incoupled power and the alignment of the ridge devices, is quite challenging for this geometry. Due to the low resistances of the devices, the electrical measurements required careful data analysis and interpretation. We see that the reduction of the number of periods effectively increases the device responsivity, with the drawback of a decrease in device resistance. Future challenges include the simulation and design of a single-period structure with a higher zero-bias resistance at room temperature in order to improve its noise behaviour and thus its usability in photonic integrated circuits.

Funding. Horizon 2020 Framework Programme (828893); Austrian Science Fund (M2485-N34); Air Force Office of Scientific Research (FA8655-22-1-7170); Österreichische Forschungsförderungsgesellschaft (883941).

Acknowledgments. The authors want to acknowledge fruitful scientific discussions with W. Schrenk and E. Gornik.

Disclosures. The authors declare no conflicts of interest.

Data availability. Data underlying the results presented in this paper are not publicly available at this time but may be obtained from the authors upon reasonable request.

Supplemental document. See [Supplement 1](#) for supporting content.

References

1. A. Harrer, R. Szedlak, B. Schwarz, H. Moser, T. Zederbauer, D. MacFarland, H. Detz, A. M. Andrews, W. Schrenk, B. Lendl, and G. Strasser, "Mid-infrared surface transmitting and detecting quantum cascade device for gas-sensing," *Sci. Rep.* **6**(1), 21795 (2016).
2. A. Dabrowska, M. David, S. Freitag, A. M. Andrews, G. Strasser, B. Hinkov, A. Schwaighofer, and B. Lendl, "Broadband laser-based mid-infrared spectroscopy employing a quantum cascade detector for milk protein analysis," *Sens. Actuators, B* **350**, 130873 (2022).
3. C. Tomasi and F. Tampieri, "Size distribution models of small water droplets in mist and their volume extinction coefficients at visible and infrared wavelengths," *Atmos. Environ.* (1967) **10**(11), 1005–1013 (1976).
4. B. Hinkov, A. Hugi, M. Beck, and J. Faist, "Rf-modulation of mid-infrared distributed feedback quantum cascade lasers," *Opt. Express* **24**(4), 3294–3312 (2016).
5. H. Dely, T. Bonazzi, O. Spitz, E. Rodriguez, D. Gacemi, Y. Todorov, K. Pantzas, G. Beaudoin, I. Sagnes, L. Li, A. G. Davies, E. H. Linfield, F. Grillot, A. Vasanelli, and C. Sirtori, "10 gbit/s free space data transmission at $9\ \mu\text{m}$ wavelength with unipolar quantum optoelectronics," *Laser Photonics Rev.* **16**(2), 2100414 (2022).
6. A. Soibel, M. W. Wright, W. H. Farr, S. A. Keo, C. J. Hill, R. Q. Yang, and H. C. Liu, "Midinfrared interband cascade laser for free space optical communication," *IEEE Photonics Technol. Lett.* **22**(2), 121–123 (2010).
7. B. Levine, K. Choi, C. Bethea, J. Walker, and R. Malik, "New $10\ \mu\text{m}$ infrared detector using intersubband absorption in resonant tunneling GaAlAs superlattices," *Appl. Phys. Lett.* **50**(16), 1092–1094 (1987).
8. D. Palaferri, Y. Todorov, A. Bigioli, A. Mottaghizadeh, D. Gacemi, A. Calabrese, A. Vasanelli, L. Li, A. G. Davies, E. H. Linfield, F. Kapsalidis, M. Beck, J. Faist, and C. Sirtori, "Room-temperature nine- μm -wavelength photodetectors and GHz-frequency heterodyne receivers," *Nature* **556**(7699), 85–88 (2018).
9. H. Liu, J. Li, M. Buchanan, and Z. Wasilewski, "High-frequency quantum-well infrared photodetectors measured by microwave-rectification technique," *IEEE J. Quantum Electron.* **32**(6), 1024–1028 (1996).
10. M. Graf, N. Hoyler, M. Giovannini, T. Aellen, J. Faist, and D. Hofstetter, "Mid-infrared quantum cascade detectors on InP," in *Infrared and Photoelectronic Imagers and Detector Devices II*, vol. 6294 (International Society for Optics and Photonics, 2006), p. 62940P.
11. D. Hofstetter, M. Beck, and J. Faist, "Quantum-cascade-laser structures as photodetectors," *Appl. Phys. Lett.* **81**(15), 2683–2685 (2002).
12. H. Schneider, C. Schönbein, G. Bihlmann, P. Van Son, and H. Sigg, "High-speed infrared detection by uncooled photovoltaic quantum well infrared photodetectors," *Appl. Phys. Lett.* **70**(12), 1602–1604 (1997).
13. J. Faist, M. Beck, T. Aellen, and E. Gini, "Quantum-cascade lasers based on a bound-to-continuum transition," *Appl. Phys. Lett.* **78**(2), 147–149 (2001).
14. M. David, A. Dabrowska, M. Sistani, I. Doganlar, E. Hinkelmann, H. Detz, W. Weber, B. Lendl, G. Strasser, and B. Hinkov, "Octave-spanning low-loss mid-IR waveguides based on semiconductor-loaded plasmonics," *Opt. Express* **29**(26), 43567–43579 (2021).

15. B. Schwarz, P. Reininger, D. Ristanić, H. Detz, A. M. Andrews, W. Schrenk, and G. Strasser, "Monolithically integrated mid-infrared lab-on-a-chip using plasmonics and quantum cascade structures," *Nat. Commun.* **5**(1), 4085 (2014).
16. B. Hinkov, F. Pilat, L. Lux, P. L. Souza, M. David, A. Schwaighofer, D. Ristanić, B. Schwarz, H. Detz, A. M. Andrews, B. Lendl, and G. Strasser, "A mid-infrared lab-on-a-chip for dynamic reaction monitoring," *Nat. Commun.* **13**(1), 4753 (2022).
17. Z. Zhang, Y. Xiao, Z. Ma, M. Xiao, Z. Ding, X. Lei, G. K. Karagiannidis, and P. Fan, "6G wireless networks: Vision, requirements, architecture, and key technologies," *IEEE Veh. Technol. Mag.* **14**(3), 28–41 (2019).
18. M. Giordani, M. Polese, M. Mezzavilla, S. Rangan, and M. Zorzi, "Toward 6G networks: Use cases and technologies," *IEEE Commun. Mag.* **58**(3), 55–61 (2020).
19. N. Witternigg, M. Schönhuber, E. Leitgeb, and T. Plank, "Feasibility assessment of optical technologies for reliable high capacity feeder links," *Acta Astronaut.* **89**, 254–260 (2013).
20. X. Pang, O. Ozolins, L. Zhang, R. Schatz, A. Udalcovs, X. Yu, G. Jacobsen, S. Popov, J. Chen, and S. Lourdudoss, "Free-space communications enabled by quantum cascade lasers," *Phys. Status Solidi A* **218**(3), 2000407 (2021).
21. B. Hinkov, A. Bismuto, Y. Bonetti, M. Beck, S. Blaser, and J. Faist, "Singlemode quantum cascade lasers with power dissipation below 1 W," *Electron. Lett.* **48**(11), 646–647 (2012).
22. T. Plank, E. Leitgeb, P. Pezzei, and Z. Ghassemlooy, "Wavelength-selection for high data rate free space optics (FSO) in next generation wireless communications," in *2012 17th European Conference on Networks and Optical Communications*, (2012), pp. 1–5.
23. S. Blaser, D. Hofstetter, M. Beck, and J. Faist, "Free-space optical data link using peltier-cooled quantum cascade laser," *Electron. Lett.* **37**(12), 778–780 (2001).
24. M. Taslakov, V. Simeonov, and H. Van den Bergh, "Line-of-sight data transmission system based on mid IR quantum cascade laser," in *Free-Space Laser Communication Technologies XX*, vol. 6877 (International Society for Optics and Photonics, 2008), p. 68770F.
25. J. Mikołajczyk, D. Szabra, A. Prokopiuk, K. Achtenberg, J. Wojtas, and Z. Bielecki, "Optical wireless communications operated at long-wave infrared radiation," *Int. J. Electron. Telecommun.* **66**(2), 383–387 (2020).
26. M. Garlinska, A. PREGOWSKA, I. Gutowska, M. Osial, and J. Szczepanski, "Experimental study of the free space optics communication system operating in the 8–12 μm spectral range," *Electronics* **10**(8), 875 (2021).
27. B. Schwarz, P. Reininger, H. Detz, T. Zederbauer, A. M. Andrews, W. Schrenk, and G. Strasser, "Monolithically integrated mid-infrared quantum cascade laser and detector," *Sensors* **13**(2), 2196–2205 (2013).
28. Y. Zou, K. Vijayraghavan, P. Wray, S. Chakravarty, M. A. Belkin, and R. T. Chen, "Monolithically integrated quantum cascade lasers, detectors and dielectric waveguides at 9.5 μm for far-infrared lab-on-chip chemical sensing," in *CLEO: Science and Innovations*, (Optical Society of America, 2015), pp. STu4I–2.
29. A. Harrer, B. Schwarz, R. Gansch, P. Reininger, H. Detz, T. Zederbauer, A. M. Andrews, W. Schrenk, and G. Strasser, "Plasmonic lens enhanced mid-infrared quantum cascade detector," *Appl. Phys. Lett.* **105**(17), 171112 (2014).
30. P. Reininger, B. Schwarz, R. Gansch, H. Detz, D. MacFarland, T. Zederbauer, A. Andrews, W. Schrenk, and G. Strasser, "Quantum cascade detector utilizing the diagonal-transition scheme for high quality cavities," *Opt. Express* **23**(5), 6283–6291 (2015).
31. A. Jollivet, B. Hinkov, S. Pirotta, H. Hoang, S. Derelle, J. Jaeck, M. Tchernycheva, R. Colombelli, A. Bousseksou, M. Hugues, N. Le Biavan, J. Tamayo-Arriola, M. Montes Bajo, L. Rigutti, A. Hierro, G. Strasser, J.-M. Chauveau, and F. H. Julien, "Short infrared wavelength quantum cascade detectors based on m-plane ZnO/ZnMgO quantum wells," *Appl. Phys. Lett.* **113**(25), 251104 (2018).
32. S. Sakr, P. Crozat, D. Gacemi, Y. Kotsar, A. Pesach, P. Quach, N. Isac, M. Tchernycheva, L. Vivien, G. Bahir, E. Monroy, and F. H. Julien, "GaN/AlGaIn waveguide quantum cascade photodetectors at lambda approximate to 1.55 μm with enhanced responsivity and similar to 40 GHz frequency bandwidth," *Appl. Phys. Lett.* **102**(1), 011135 (2013).
33. M. Helm, "The basic physics of intersubband transitions," in *Semiconductors and semimetals*, vol. 62 (Elsevier, 1999), pp. 1–99.
34. M. Giparakis, H. Knötig, H. Detz, M. Beiser, W. Schrenk, B. Schwarz, G. Strasser, and A. M. Andrews, "2.7 μm quantum cascade detector: Above band gap energy intersubband detection," *Appl. Phys. Lett.* **120**(7), 071104 (2022).
35. A. Delga, "Quantum cascade detectors: A review," in *Mid-infrared Optoelectronics*, (Woodhead Publishing, 2020), Woodhead Publishing Series in Electronic and Optical Materials, pp. 337–377.
36. B. Schwarz, P. Reininger, A. Harrer, D. MacFarland, H. Detz, A. M. Andrews, W. Schrenk, and G. Strasser, "The limit of quantum cascade detectors: A single period device," *Appl. Phys. Lett.* **111**(6), 061107 (2017).
37. P. Enders and M. Woerner, "Exact block diagonalization of the eight-band hamiltonian matrix for tetrahedral semiconductors and its application to strained quantum wells," *Semicond. Sci. Technol.* **11**(7), 983–988 (1996).
38. B. A. Foreman, "Elimination of spurious solutions from eight-band $\mathbf{k} \cdot \mathbf{p}$ theory," *Phys. Rev. B* **56**(20), R12748 (1997).
39. M. A. Panah, L. Han, K. Norrman, N. Pryds, A. Nadtochiy, A. Zhukov, A. Lavrinenko, and E. Semenova, "Mid-IR optical properties of silicon doped InP," *Opt. Mater. Express* **7**(7), 2260–2271 (2017).